Earthquake surface ruptures on the altiplano and geomorphological evidence of normal faulting in the December 2016 (Mw 6.1) Parina earthquake, Peru

Enoch Aguirre [a], Carlos Benavente [a,e,*], Laurence Audin [b], Sam Wimpenny [c], Stéphane Baize [d], Lorena Rosell [a], Fabrizio Delgado [e], Briant García [a,e], Anderson Palomino [a]

[a] *Instituto Geológico, Minero y Metalúrgico INGEMMET, Av. Canadá 1470 San Borja, Lima-Perú, Peru*
[b] *Univ. Grenoble Alpes, Univ. Savoie Mont Blanc, CNRS, IRD, IFSTTAR, ISTerre, 38000, Grenoble, France*
[c] *COMET, Bullard Laboratories, Department of Earth Sciences, University of Cambridge, UK*
[d] *Institut de Radioprotection et de Sûreté Nucléaire (IRSN), BP 17, 92262, Fontenay-aux-Roses, France*
[e] *Especialidad Ingeniería Geológica, Facultad de Ciencias e Ingeniería. Pontificia Universidad Católica del Perú, Av. Universitaria 1801, San Miguel, Lima, 15088, Peru*

A B S T R A C T

The 2016 Mw 6.1 Parina earthquake ruptured a shallow-crustal normal fault within the high Andes of south Peru. We use high-resolution DEMs and field mapping of the surface ruptures generated by the earthquake, in combination with **co-seismic** and **post-seismic** InSAR measurements, to investigate how different features of the geomorphology at Parina are generated by the earthquake cycle on the Parina Fault. We systematically mapped 12 km of NW-SE trending surface ruptures with up to ~27 cm vertical displacement and ~25 cm tensional opening along strike, separated by a gap with no observable surface ruptures. Co- and post-seismic InSAR measurements require slip below this gap in surface ruptures, implying that surface offsets observed in paleoseismic trenches may not **necessarily be** representative of slip at seismogenic depths, and will typically yield an underestimate of paleo-earthquake magnitudes. The surface ruptures developed along 10–20 m high cumulative scarps cutting through late Quaternary fluvio-glacial deposits and bedrock. The 2016 Parina earthquake did not rupture the full length of the late Quaternary scarps, implying that the Parina Fault does not slip in characteristic, repeat earthquakes. At Parina, and across most of the Peruvian Altiplano, normal faults are most-easily identified from recent scarps cutting late Quaternary moraine crests. In regions where there are no **recently-deposited** moraines, faults are difficult to **identify** and **lack time constraints to quantify rates of fault slip**. **For this reason**, current fault maps may underestimate the seismic hazard **in the Altiplano**.

1. Introduction

On **the** December 1, 2016 a **rare**, shallow M_w 6.1 earthquake was recorded in the Altiplano of southern Peru near the village of Parina (Fig. 1). The epicenter was located ~50 km west of Lampa village in a remote region of the plateau, though three fatalities and damage to local infrastructure **were** recorded (Llontop and Marrou, 2016). Body-waveform seismology and radar geodetic measurements have revealed that the earthquake ruptured a ~15 km-long, NW-SE striking normal fault, **which trends sub-parallel to a well-documented system of normal faults cutting across the Altiplano known as the** Cusco-Lagunillas Fault System (CLFS) (Fig. 1a; Wimpenny et al., 2018; Xu et al., 2019; Sébrier et al., 1985a,b; Benavente et al., 2013). Although an active fault map for the Peruvian Andes has been released by INGEMMET (Macharé et al., 2009; Benavente et al., 2013; *2017*; *INGEMMET, 2017*), **the Parina earthquake ruptured a previously-unmapped structure. This event provides a unique**

opportunity to assess how key features of an earthquake, such as the fault location and the slip distribution, are related to the geomorphology and surface ruptures in the epicentral region, and to examine how earthquakes are preserved in the Altiplano landscape.

Whether fault-related geomorphology, such as fault scarps, accurately reflect the distribution of slip in past earthquakes is a particularly pertinent question for seismic hazard assessment in slowly-deforming regions like the Peruvian Altiplano. Seismicity in southern Peru is infrequent enough that the modern instrumental catalogue is a poor representation of the spatial distribution of active faults and the possible maximum magnitude of earthquakes on these faults, therefore paleoseismological methods must be used to compliment the modern and historical catalogues (e.g. *Schwartz, 1988*). However, there are a number of limitations to using paleoseismological methods to infer past earthquake slip distributions and magnitudes (e.g. *Ainscoe* et al., *2018*). For example, the fault

---

scarps generated by the two moderate-magnitude earthquakes to have occurred in the Peruvian Andes prior to the Parina event – the 1946 Ms 6.4 Ancash earthquake and the 1969 Mw 6.9 Huayta-pallana (Pariahuanca) earthquake – both produced highly-segmented surface rupture traces with cumulative lengths far shorter than might be expected for earthquakes of their size (Wells and Coppersmith, 1994). The Ancash earthquake produced two 5 km-long sections of normal-faulting surface ruptures along the crest of Cerro Llamacorral, separated by a 12 km gap coincident with intervening river valleys (Bellier et al., 1991). Whilst the sur-face ruptures along the Huaytapallana Fault consisted of distinct segments 10 km-long and 6 km-long, separated by a 4 km-wide gap (*Philip and Megard, 1977*). From these rupture observations alone, it would not be possible to tell whether the gaps in the surface rupture traces reflected real along-strike variations in fault slip (e. g. due to a rupture barrier), erosional features, or a change in the material properties of the near-surface material. One way to assess

this particular limitation is by studying how slip in modern earthquakes relates to their surface ruptures and cumulative fault scarps.

In this study, **we use new field measurements of the Parina earthquake surface ruptures, coupled with high-resolution DEMs of the cumulative fault scarps formed using drone photogram-metry,** to examine the geomorphological evidence for faulting at Parina. **We compare our scarp observations** with previously-published mea-surements of co- and post-seismic ground deformation in the 2016 Parina earthquake from interferometric synthetic aperture radar (InSAR), to investigate how fault slip at depth relates to scarp formation and fault-related geomorphology at the surface. **The accuracy and relative completeness of the surface rupture dataset, including field measurement and high-resolution DEM, also provides a unique opportunity to enrich the worldwide dataset of surface ruptures (SURE)** (Baize et al., 2020).
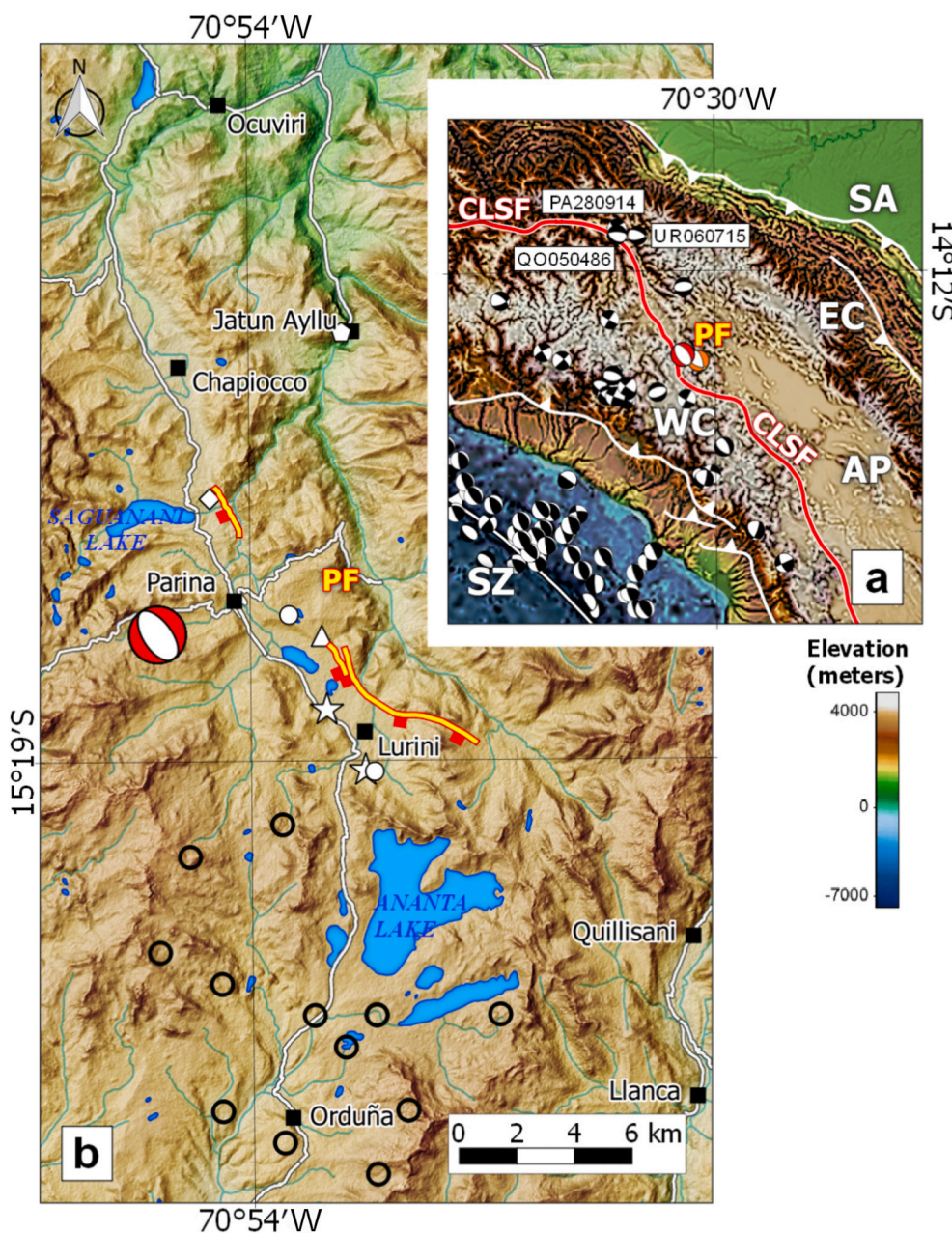

Fig. 1. a) Overview map of the Parina Fault scarp (in red). Inset (upper right) shows plate boundary setting, where (SA) Sub-andean zone, (EC) Eastern Cordillera, (AP) Altiplano, (WC) Western Cordillera, (SZ) Trench, (CLFS) for Cusco-Lagunillas Fault System and (PF) Parina Fault. The focal mechanisms seismic events shallower than 40 km hypocenter depth, with the red focal mechanism corresponding to the Parina earthquake, and the orange focal mechanism being an aftershock the next day. Note the events of Qoricocha (QO050486), Paruro (280,914) and Urcos (060,715) next to Cusco-Lagunillas Fault System (CLFS). All mechanisms are taken from the GCMT catalogue of Ekström et al. (2012) b) Close up view of the Parina Fault. White markers show the location of coseismic rock falls (pentagon), landslides (rhombus), soil liquefaction (circle), jumping stones (trian-gle) and crack openings (**five**-pointed star). Earthquake epicenters and aftershocks of the 2016 earthquake are shown as open circles. (For interpretation of the references to color in this figure legend, the reader is referred to the Web version of this article.)

2. Geological and seismotectonic setting

The Parina earthquake occurred within **the northern** Altiplano, a 350-450 km-wide plateau that extends ~1800 km along the backbone of the Andes, from southern Peru to northern Argentina. The **Peruvian** Altiplano is a low-relief basin at an average elevation of ~4500 m filled with Cenozoic sedimentary and volcaniclastic rocks that have been faulted and folded throughout the Miocene. **Internal drainage and low topographic gradients in this region have precluded any deep fluvial dissection of the landscape, though periodic glaciation over the last ~100 ka has formed U-shaped valleys, moraines and drift sheets that dominate the surface morphology.**

One of the most prominent structural features of the Peruvian Altiplano is the Cusco-Lagunillas Fault System (**CLFS**) (*Ellison* et al., *1989; Jaillard and Santander, 1992; Carlotto, 1998*). The CLFS **consists of a series of ~10–20 km-long, NW-SE trending normal faults** (Fig. 1a) **recognizable from their narrow hanginwall basins bound by uplifted and incised footwalls, as well as through Holocene fault scarps that often cut the Late Glacial Maximum moraines** (Sébrier et al., 1985b; Mercier et al., 1992; Benavente et al., 2013a; Wimpenny et al., 2020). **Modern seismicity along the CLFS is sparse.** Previous seismotectonic studies indicated that the northern **section of the CLFS near Cusco** had undergone extension in a Mb 5.3 normal-faulting earthquake that generated **minor** surface ruptures in 1986 (*Cabrera and Sébrier, 1998*) (see focal mechanism QO050486 in Fig. 1a). **The only** other moderate-magnitude (**i.e. Mw > 5**) earthquakes along the CLFS **in the instrumental catalogue did** not generate observable surface ruptures (see focal mechanism PA280914 and UR060715 in Fig. 1a). **There have also been a number of historical reports of significant earthquakes along the CLFS, with Cusco being severely damaged in 1650 and 1950, as well as a cluster of earthquakes between 1939 and 1943 that damaged settlements further south-east along the Vilcanota river valley section of the CLFS** (Ericksen et al., 1954; Silgado, 1978). **The Parina earthquake is the first known $M_w > 6$ earthquake to rupture the CLFS in the modern instrumental era.**
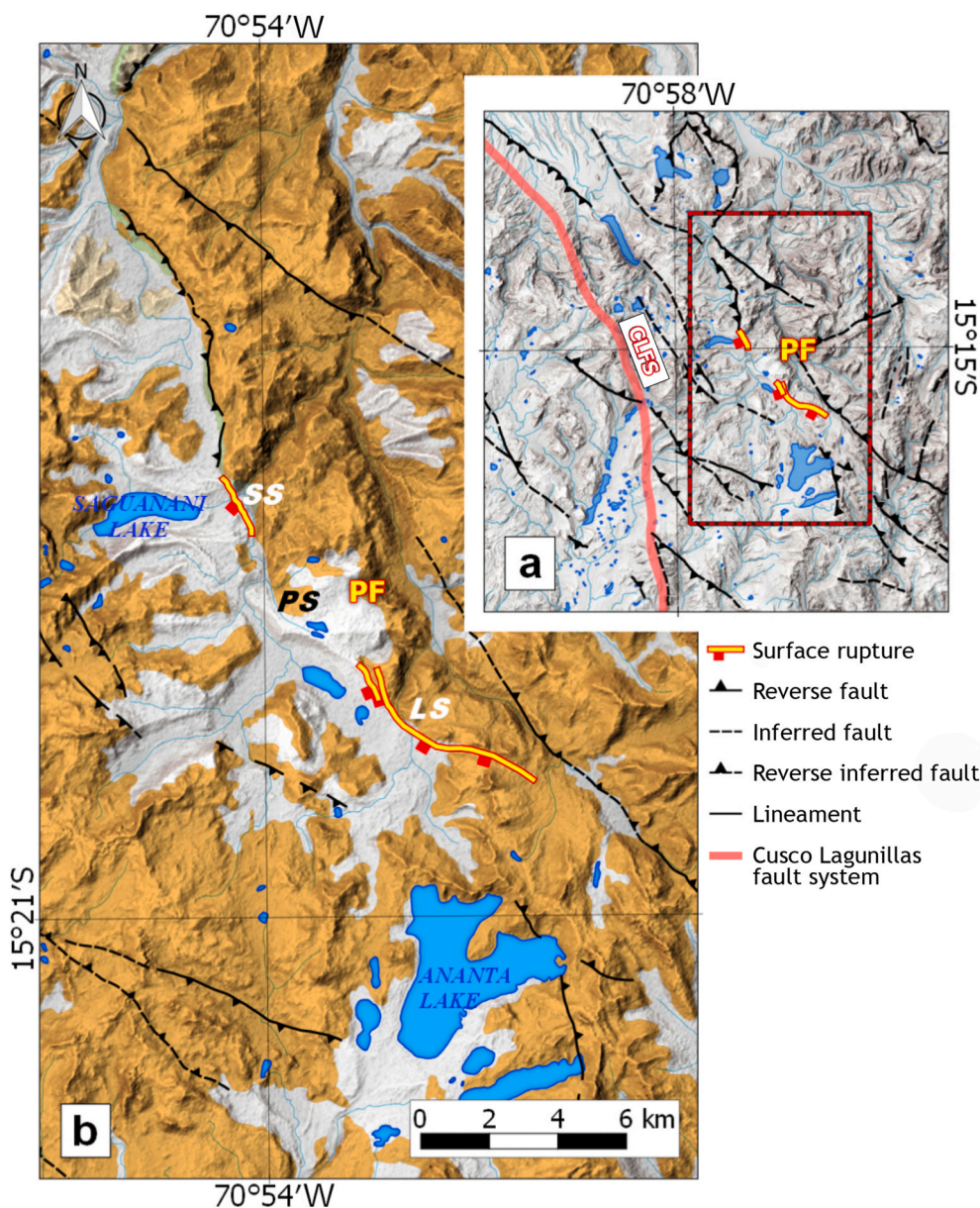

Fig. 2. a) **Structural map in the Parina epicentral region.** Inset (upper right), shows the Parina fault location respect to Cusco-Lagunillas Fault System (CLFS). b) Geology setting map (modified from *INGEMMET, 2017*). **The yellow color represents Cenozoic volcanic rocks, while the gray color represents Quaternary deposits.** Reverse faults are toothed black lines and the location of the surface rupture of 2016 event is shown by **red and yellow** line. Also shown are the segments of Parina Fault, Saguanani segment (SS), Parina segment (PS) and Lurini segment (LS). (For interpretation of the references to color in this figure legend, the reader is referred to the Web version of this article.)

3. Methods

3.1. Fieldwork

Three days after the earthquake in Parina, **we organized a post-seismic survey of** the epicentral area. On site, we mapped the surface ruptures generated by the earthquake, measured their height and tensional opening, collected an inventory of coseismic shaking effects along-strike (Fig. 3) and collected low-altitude drone imagery to form a high-resolution Digital Elevation Model (DEM), covering a surface area of ~36 km² with detailed field inspection. The field evidence of earthquake-related shaking includes tensional cracks, liquefaction, and jumping stones. No rainfall occurred within the period between the earthquake and our first field study, thus both climate and limited anthropogenic activity in the area led to excellent preservation of the earthquake surface ruptures.

3.2. DEM construction and resolution

To examine the link between the surface ruptures and the cumulative fault scarps on the Parina Fault, we constructed a high-resolution DEM along the surface-rupture trace using the structure-from-motion technique with photographs collected from an eBee senseFly drone. **The photographs** were processed with the **photogrammetry** software Agisoft Photoscan (Agisoft, 2017). Ground control points were measured using differential GPS and used to guide the image matching and georeferencing. The resulting DEM has a 20 cm horizontal resolution and a ~1 cm vertical resolution between adjacent points (Westoby et al., 2012), and is complemented with orthomosaic color imagery at 4 cm/pixel resolution along the whole length of the surface ruptures (see Fig. 3b and c).

4. Observations

4.1. Surface ruptures and environment effects of the 2016 Parina earthquake

The surface ruptures generated by the Parina earthquake consisted of two NW-SE trending segments separated by a gap of 4 km, which we call the **Parina Gap** (Fig. 3a). The northern segment of surface ruptures (the Saguanani Segment, SS) is ~2 km long, whilst the southern segment (the Lurini Segment, LS) is ~6 km long, with both being defined by a semi-continuous trace of ruptures offsetting the surface sediment and bedrock.

4.1.1. Saguanani and Lurini segments

The Saguanani Segment, located at the northern end of the Parina Fault, displayed average vertical offsets across the surface ruptures of 3 cm, with maximum vertical offsets up to 8 cm (Figs. 4c and 5). The surface ruptures formed a series of sub-parallel, overlapping **strands that are best** preserved in sag ponds formed in the interfluves between E-W trending moraine crests. The surface ruptures terminate at their southern end where they intersect a ~NW-SE trending stream, and their northern termination occurs at the northern-most limit of lateral moraines around Lake Saguanani.

The Lurini **S**egment preserved far larger vertical and tensional offsets across the ruptures of up to 27 cm (Fig. 4a and b). Vertical and horizontal displacements across the ruptures decrease from a maximum in the middle of the Luruni **S**egment to a minimum at the tips of the segment **with a slip-length ratio of 5×10^{-5}**, matching the classic triangular shape expected for active normal faults (Cowie and Scholz, 1992) (see Fig. 5a and b). The northern ~750 m of the Luruni Segment consists of overlapping, sub-parallel strands of ruptures, whilst towards the south-east the remaining ~5 km of ruptures follow a single, curvi-linear trace. The northern termination of the ruptures in the Luruni **S**egment occurs in a region coincident with sag small ponds and evidence for liquefaction, whilst the southern termination of the surface ruptures occurs where the fault trace crosses a stream.
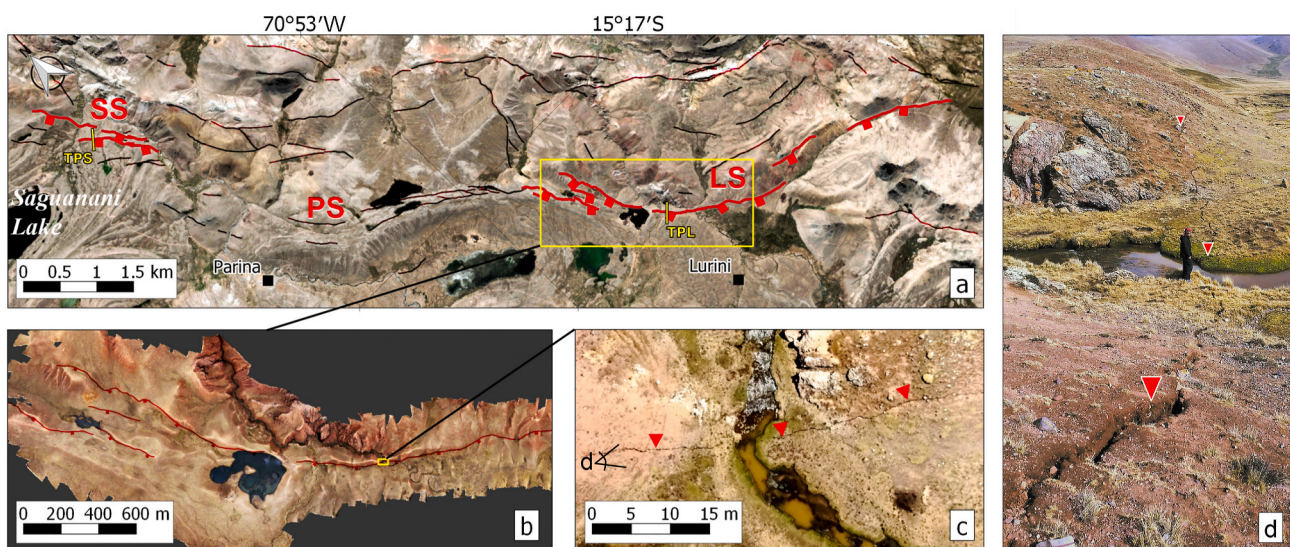

Fig. 3. a) Optical satellite imagery (from Google, DigitalGlobe) showing in red lines the Parina fault segments: Saguanani segment (SS), Parina segment (PS) and Lurini segment (LS). Black lines are Holocene tectonics scarps mapped during field work. Note that in the Parina segment there is no surface rupture trace. b) Red relief image map (RRIM) derived from the DEM (Chiba et al., 2007, 2008), built with photogrammetric surveyed data along the surface rupture (this study). Red lines are highlighting the surface rupture surveyed by foot along the fault trace. The location of the high-resolution DEM is highlighted by the yellow box in (a). c) Aerial photograph from the flying Ebee (4 cm in resolution). The footwall (top) and hanging wall (bottom) are limited by the scarp indicated by red triangles, note the scarp is cut by a stream, its flow direction is from south to north. The location of this drone image is outlined as a yellow box on (b). d) Surface offset associated to Parina earthquake; picture **taken** from western stream margin looking south-east along the scarp. Location is displayed in "d" letter in (c). (For interpretation of the references to color in this figure legend, the reader is referred to the Web version of this article.)

Fig. 4. Field photographs of coseismic surface ruptures and associated shaking effects. a) ~10 cm surface rupture, located in Lurini segment. b) ~27 cm surface rupture, located in Lurini segment. c) ~20 cm crack opening, located in Lurini segment. d) Sand boils west of the lake in Parina segment. e) Jumping stones, which are co-located with the sand boils, in Parina segment. f) Rockfall, which dammed the Jatun Ayllu River, some 12 km north of the epicenter. Note that near to surface rupture there is no more rock fall, probably due to the limited relief. See the yellow circle for the scale. (For interpretation of the references to color in this figure legend, the reader is referred to the Web version of this article.)
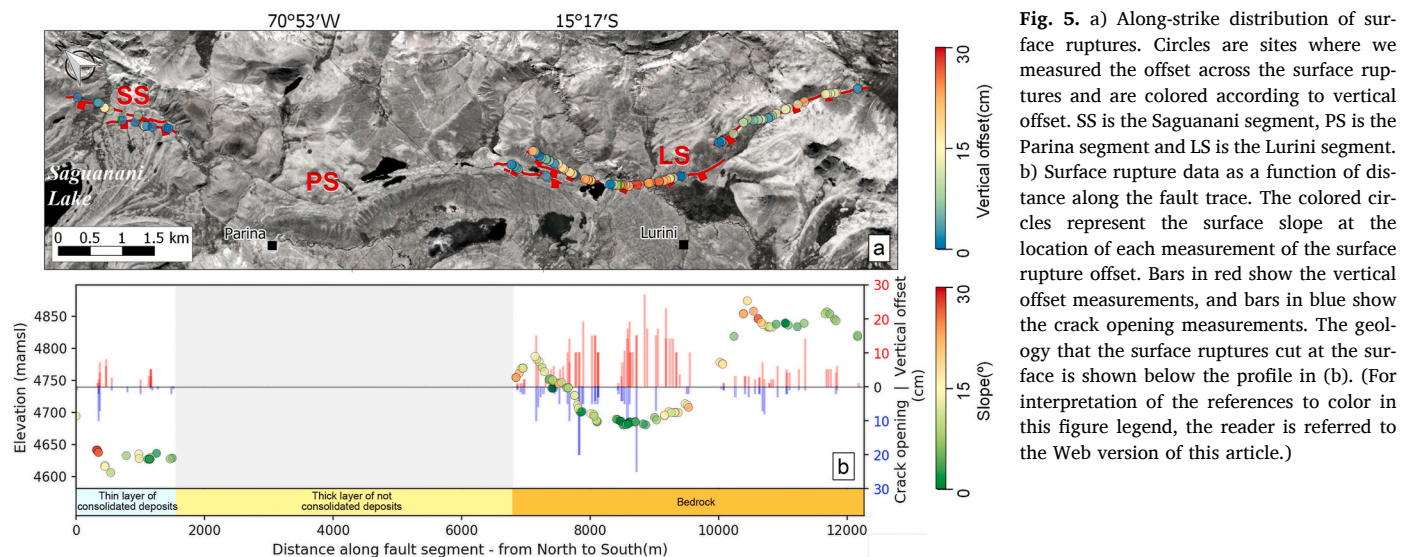
Fig. 5. a) Along-strike distribution of surface ruptures. Circles are sites where we measured the offset across the surface ruptures and are colored according to vertical offset. SS is the Saguanani segment, PS is the Parina segment and LS is the Lurini segment. b) Surface rupture data as a function of distance along the fault trace. The colored circles represent the surface slope at the location of each measurement of the surface rupture offset. Bars in red show the vertical offset measurements, and bars in blue show the crack opening measurements. The geology that the surface ruptures cut at the surface is shown below the profile in (b). (For interpretation of the references to color in this figure legend, the reader is referred to the Web version of this article.)

Along the Saguanani and Luruni Segments, the landscape has a low relief, and we did not observe any superficial mass movements with uphill extensional scars and downhill compressional bulges. A slope map generated from the high-resolution DEM shows that the slopes around the surface ruptures are below 15° on average, and that at Luruni, where vertical displacement is greatest, the topographic slope is at its lowest <10° (Fig. 5b). As slopes in granular material are generally stable at angles of repose <30°, and the observation that regions with the highest slope angle have the smallest offsets across the surface ruptures, we believe that the first-order variations in displacement across the surface ruptures reflect variations in slip on the shallow portion of the Parina Fault, and not surface slope instability.

4.1.2. Parina Gap

Between the Saguanani and Luruni Segments there is a distinct gap in the mapped rupture trace. Although this gap does not show any evidence of surface rupture, we mapped several features that are commonly associated with near-field ground shaking within this region, such as sand boils (Fig. 4d and e) and jumping stones (Fig. 4e).

The sand boils are found within the hanging wall of the Parina Fault in areas of dry lake beds (Fig. 4d), are ~30 cm in diameter and are formed of medium-to-fine grained brown sands. In other settings, sand boils typically form through the ejection of fluidized sand through the shallow clay-rich sediments as a result of the shaking generated during an earthquake. This behavior of the near-surface sediment can last for a significant time after the seismic shaking, as the fine-grained sediments relax into a stable packing configuration and continue to expel pore waters (see *Rodríguez-Pascua* et al., 2015). The presence of sand boils within the Parina Gap is indicative of seismically-induced liquefaction around the Parina Fault in this area.

Jumping stones are volcanic boulders of ~20–30 cm diameter that are displaced laterally from their original resting place with no evidence of rolling along the sediment surface (Fig. 4e), indicating they have been lifted vertically and translated relative to the ground surface whilst in the air (e.g. *King* et al., 2018). We observe the jumping stones within the uplifted footwall of the Parina Gap and find they are consistently translated ~20–30 cm towards the south-east, which is roughly parallel to the fault trace inferred from the Saguanani and Luruni surface ruptures. For the stones to leave the ground surface means that the vertical ground acceleration exceeded 1 g during the earthquake. In addition, there must have been some horizontal component to the ground velocity either during the instant the stones left the ground surface, or whilst the stones were in the air.

4.1.3. Landsliding and rockfalls

The area near Parina is characterised by gentle relief. Nonetheless, we observed gravitational processes such as rock falls and small landslides in the epicentral region, in particular the Jatun Ayllu ravine (Fig. 1). This rockfall was located 13 km from the epicentral and covered a total area of ~0.60 km^2 (Fig. 4f). Rock falls were constituted of individual boulders or disrupted m-scale boulders (up to 10 m high) that descended slopes by rolling, jumping or free fall. This type of landslide was less common in comparison to shallow, disrupted landslides.

4.2. *Late quaternary fault scarps on the Parina Fault*

The surface ruptures formed in the 2016 Parina earthquake consistently follow ~5 to 20 m-high, pre-existing scarps cutting bedrock, alluvium and glacial deposits along the base of a ~150 m-high escarpment that marks the footwall of the Parina Fault. If these metre-high scarps are formed by repeated slip on the Parina Fault, the scarp heights correspond to a minimum vertical tectonic offset since the last period of glacial resurfacing and moraine formation at Parina. Exposure and radiocarbon dating of moraines in the nearby Cordillera Vilcanota suggest the last major episode of moraine deposition occurred during the Last Glacial Maximum ~10–45 ka (Clapperton, 1983), roughly placing the moraines and scarps as late Quaternary in age.

We used the high-resolution DEM to map the late Quaternary fault scarps and find that their along-strike distribution is similar to the surface ruptures generated by the 2016 Parina earthquake, but with some subtle differences (Fig. 7a,7 b). At Saguanani, the late Quaternary scarps form a series of sub-parallel strands that have offset the crests of nested lateral moraines and are directly coincident with the surface ruptures. We did not identify any late Quaternary scarps preserved in the Parina Gap – the same region there were no surface ruptures. In the Luruni Segment, late Quaternary fault scarps do outcrop along much of the surface rupture trace, but extend ~1 km further north-west than the 2016 surface ruptures, and do not occur along the ~1.5 km of the south-eastern end of the rupture trace.

The **also** extracted a series of topographic profiles across the late Quaternary fault scarps from our high-resolution DEM, **in order to compare the along-strike scarp height distribution to the surface rupture heights. We calculate the scarp heights by using least-squares regression to fit lines to points above and below the scarp, and calculated the vertical separation of these lines. In many**

places the scarp height variations may not reflect variations in fault throw, as erosional scouring within the hanging wall by axially-draining streams and deposition within small sag ponds may **mask** fault throw variations. We therefore only estimated scarp heights on selected surfaces that could be reliably correlated across the fault, such as moraine crests and abandoned fan surfaces (Fig. 6). **As a result of this selective sampling,** the along-strike distribution of late Quaternary scarp height measurements is far sparser than the surface rupture height distribution (compare Fig. 7d and e).

In the Saguanani Segment, we summed the vertical offsets **across the sub-parallel fault scarps cutting late Quaternary moraine crests to estimate the cumulative vertical offset is between 5 and 15 m at different points along-strike.** In the Luruni Segment

there are fewer places to make reliable scarp measurements, but the scarps are between 5 and 10 m-high. In contrast with the along-strike distribution of surface rupture heights in the 2016 Parina earthquake, the late Quaternary scarp heights do not increase towards the center of the Luruni Segment (Fig. 7d and e). **Areas where the surface ruptures had the highest vertical offset and tensional opening do not necessarily correspond to where the Quaternary fault scarps were highest.**
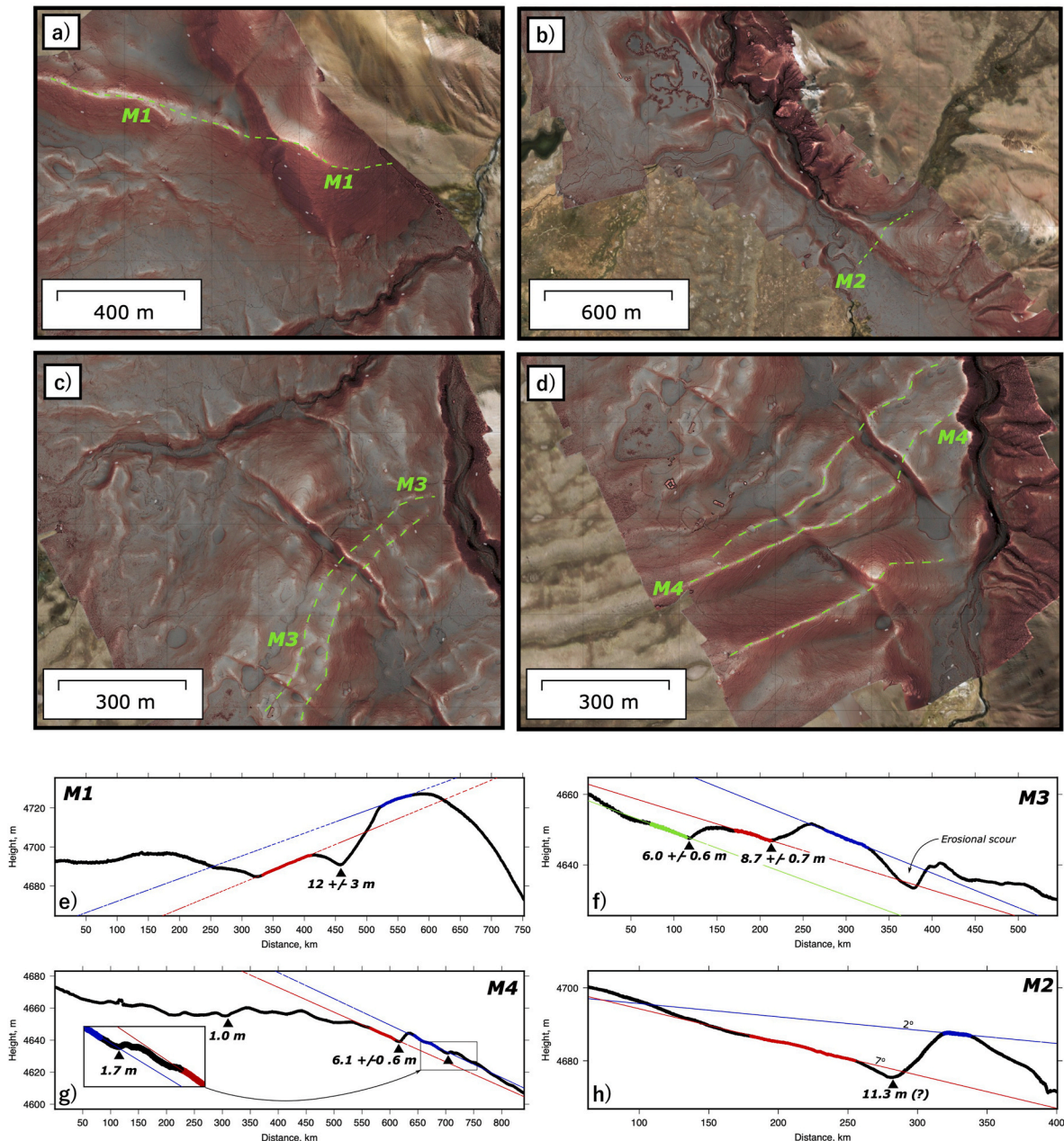

Fig. 6. Topographic profiles across the late Quaternary fault scarps extracted from high-resolution DEM. (a–d) Relief maps of the Parina late Quaternary scarps in the Saguanani (a,c,d) and Luruni (b) segments. Dashed green lines indicate profiles along surfaces or moraine crests that have been offset by the fault. Example topographic profiles are shown below. On the profiles, lines have been fit in a least-squares sense to points in the hangingwall (red) and footwall (blue), and the scarp height is measured as the vertical offset between these lines at the foot of the scarp. On low-dip angle surfaces (<10°), the scarp height is similar to the fault throw to within ±15%. (For interpretation of the references to color in this figure legend, the reader is referred to the Web version of this article.)
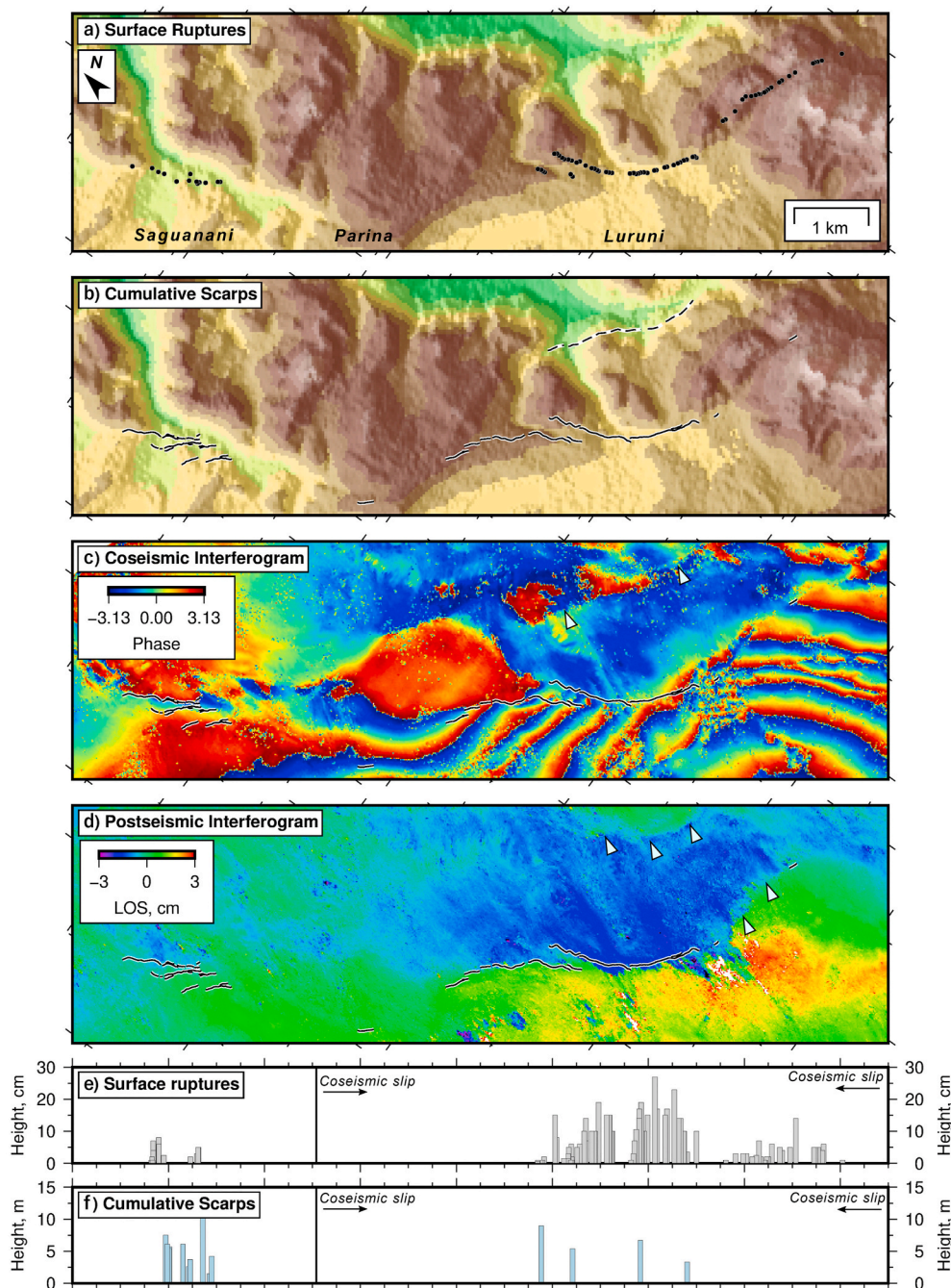
Fig. 7. Comparison of the topography with the surface ruptures, late Quaternary scarps, coseismic and **post-seismic** surface displacements. (a) SRTM 30 m topography with the mapped surface ruptures shown as black dots. (b) The same topography with mapped late Quaternary scarps shown as black lines. (c) Wrapped descending-track coseismic interferogram. (d) Unwrapped descending-track **post-seismic** interferogram between December 20, 2016 and June 30, 2017. (e) Along-strike distribution of coseismic surface rupture heights. (f) Along-strike distribution of cumulative scarp heights measured from offset moraine crests and fan surfaces using the high-resolution DEM.

5. Discussion

5.1. *Surface ruptures, late quaternary scarps and slip on the Parina Fault*

In this section we present a comparison between the surface ruptures and late Quaternary scarp heights mapped in this study, and the co- and post-seismic surface deformation recorded by InSAR from *Wimpenny et al. (2018)* to study how co- and post-seismic fault slip contribute to surface rupture formation and fault scarp growth.

The coseismic interferograms captured a relatively smooth pattern of surface displacement in the earthquake with 5–6 concentric fringes in the interferometric wrapped phase to the southwest of the mapped surface ruptures corresponding to ~15–20 cm of line-of-sight motion. Patches of low coherence in the interferogram visible as speckle within the fault hangingwall coincide with a marshy area that may have

undergone significant liquefaction (Fig. 7d). Interferogram fringes are truncated in the location of the surface ruptures on the Luruni Segment, but not on the Saguanani Segment, indicating that more slip reached the shallow fault zone at Luruni than Saguanani. In addition, the peak line-of-sight displacement at the center of the fringe pattern directly correlates with the location of the highest surface ruptures (Fig. 7c,e).

Wimpenny et al. *(2018)* and *Xu* et al. *(2019)* inverted the coseismic InSAR measurements for the geometry of the Parina Fault and the distribution of fault slip in the earthquake. Both studies found that the majority of fault slip (~50–70 cm) occurred between 3 and 10 km depth beneath the central Luruni Segment, whilst the InSAR data do not require any coseismic fault slip beneath the Saguanani Segment. Neither study required there to be slip within the top 2 km of the fault zone at any point along-strike, leading to the inference of a 'shallow slip deficit' (e.g. *Fialko* et al., *2005*; *Xu* et al., *2019*). However, the fault dip

determined from the kinematic slip inversions (40°) and the maximum surface rupture height (27 cm) requires there was at least 35 cm of slip in parts of the shallow fault zone, highlighting the widely-recognized limitation of kinematic slip inversions using an elastic half-space Green's Function to accurately capture small-scale variations in near-surface fault slip.

Post-seismic slip may also contribute to the formation of surface ruptures and scarps. Post-seismic surface displacements measured from InSAR (Fig. 7d) indicate that the Luruni segment experienced ~7 cm of shallow afterslip between 0 and 3 km depth in the year following the earthquake coincident with the surface rupture trace (Wimpenny et al., 2018). Beneath the central part of the Parina Gap, ~2–4 cm of afterslip remained buried between ~2 and 5 km and did not reach the surface (Xu et al., 2019). There is little evidence for post-seismic deformation in the Saguanani Segment that could be related to shallow afterslip (Fig. 7d).

The comparison between the InSAR measurements, surface ruptures and fault scarps highlights a number of key features: (1) co- and post-seismic fault slip did occur at depth beneath the gap in the surface rupture trace, but this slip did not propagate to the surface in the 2016 earthquake, or in any scarp-forming earthquakes in the late Quaternary, (2) despite there being no resolvable co- or post-seismic slip beneath the surface ruptures of the Saguanani segment, late Quaternary scarps cutting lateral moraine crests in this area indicate there has been significant slip on this section of the Parina Fault in the late Quaternary, and (3) shallow post-seismic deformation can contribute a significant fraction (~20%) of fault scarp and surface rupture heights.

5.2. *Preservation of surface ruptures, late quaternary scarps and surface geology*

The kinematics and distribution of the surface ruptures and fault scarps at Saguanani and Lurini are independent of the topography, but vary along-strike in a manner that is not related to the first-order variation of slip at depth derived from the InSAR measurements. The prime example of this behavior is beneath the Parina Gap. There are subtle differences between the surface geology and conditions in the Saguanani-Lurini segments and the Parina **Gap** that may account for the along-strike variations in surface rupture and fault scarp preservation. At Saguanani and Luruni the surface geology consists of a thin veneer of unconsolidated sediments, including Last Glacial Maximum moraines and Pleistocene fluvio-glacial deposits that cover the bedrock, which can be seen exposed where streams cut through the fault footwall (Fig. 2b). In contrast, along the central Parina Gap, the extrapolated fault trace would cut through depressions filled with lacustrine and fluvio-glacial sediments dotted with small water bodies, suggesting the ground may be saturated in the near surface. We found evidence for this saturation when we attempted to trench a section of the fault near the north-western tip of the Luruni segment.

It seems likely that the 2016 Parina earthquake and previous late Quaternary earthquakes did not propagate to the surface in the Parina segment, either because of the quasi-plastic mechanical properties of the unconsolidated fluvio-glacial deposits, or because much of the near-surface material in the Parina segment liquefied during the earthquake, both of which prevent discrete ruptures forming. The observation that surface ruptures are absent in regions where liquefaction features are present suggests the latter of these two suggestions may be the dominant control at Parina.

The control of surface geological conditions on coseismic surface rupture patterns is well-documented. *Khajavi* et al. *(2014)* proposed that the thickness of the cover deposits or unconsolidated sediment is an important control on surface rupture on the Hope Fault, New Zealand. During the 2016 Amatrice-Norcia earthquake sequence, *Pucci* et al. *(2017)* and *Civico et al. (2018)* observed this same effect along the Laga Mts Fault and the Monte Vettore faults. Similarly, *Moss* et al. *(2013)* and *Stanton (2013)* concluded that the likelihood of rupture propagation to the surface is controlled by parameters such as the thickness and stiffness of the surface cover.

Just as the surface ruptures are not formed everywhere up-dip of the main coseismic rupture area at depth, the late Quaternary scarps are also discontinuous along-strike and are only preserved in certain settings. At Parina, the best-preserved fault scarps are in the Saguanani **S**egment, where the fault has cut late Quaternary lateral moraines. This is a pattern recognized across much of south Peru and offers a general rule for mapping faults in the region: recently-active faults are best preserved in regions affected by recent glaciation. As the active normal faults have accommodated little finite extension, their footwalls are not always elevated relative to their hangingwall basin, and therefore the standard morphology associated with normal faults in faster-deforming parts of the world (e.g. Greece, western Turkey; *Jackson* et al., 1982; *Hubert-Ferrari* et al., 2002) is difficult to identify in the Altiplano of southern Peru. In addition, a previous phase of shortening in the late Miocene (*Perez and Horton, 2014*) has left remnant topography associated with upright anticlinal folding and footwall ridges that is often larger in amplitude than that formed by normal faulting meaning faults can be nearly impossible to identify from the regional topography alone. As a result, if most faults are only being preserved where they cut recently-deposited moraines, there is significant difficulty in understanding the along-strike continuity of the normal faults in the Peruvian Altiplano from geomorphology alone. Similarly, there is probably a significant sampling bias in fault mapping in the region related to where late Quaternary moraines are well preserved in the Altiplano.

5.3. *The Parina earthquake surface ruptures and scaling relationships*

In seismic hazard analyses, the maximum magnitude of a potential earthquake on a mapped fault is determined by comparing field observations of fault lengths and slip during individual events to empirical scaling relationships between M_w and length or slip (e.g. *Wells and Coppersmith, 1994*, hereafter W&C94). Such relationships are obtained after statistical analysis of a large number of previous events. However, there is a significant spread in the data used to construct these empirical relationships, and along-strike variations in near-surface geological conditions can significantly affect the size and outcrop of surface ruptures (Champenois et al., 2017; *Ritz et al., 2020*). Here, we compare our observations from the Parina earthquake to the W&C94 predictions.

The different values of surface rupture length (SRL), average displacement (AD) and maximum displacement (MD) for individual and combined segments are reported in Table 1. Note that to calculate the fault length including the Parina Gap, we argue that the fault remained buried at shallow depth because of the unfavorable surface geology, as suggested by the InSAR-derived coseismic source model. The final length is 12 km and we consider this to be representative of the surface rupture length in the scaling relationships.

Table 1
Data referring to the average displacement (AD), maximum displacement (MD) and the length of the surface rupture (SRL), in order to estimate the magnitude with Wells and Coppersmith (1994) approach for Saguanani (SS) and Lurini (LS) segments independently, totally with both segments and plus with Parina segment (PS).

Segments	AD (cm)	MD (cm)	SRL (km)	Mw from AD (Normal Fault, WC94) (±0.33)	Mw from MD (Normal Fault, WC94) (±0.34)	Mw from SRL (Normal Fault, WC94) (±0.34)
LS	6.8	27	6	6.0	6.2	5.9
Total SS + LS	6	27	7.7	6.0	6.2	6.0
Total SS + PS + LS	5.3	27	12	6.0	6.2	6.3

This simple analysis shows that the *Wells and Coppersmith (1994)* empirical scaling between fault slip, length and the resulting earthquake magnitude is accurate when using maximum displacement, giving Mw values close to actual instrumental measurement; total surface length at the surface and shallow subsurface fault (SS + PS + LS) scenario also gives a reasonable value. Using AD provides systematically lower prediction of the earthquake magnitude (Mw 6). Our conclusion is that, for moderate magnitude earthquakes such as that at Parina, the MD or SRL parameters of W&C94 appear to provide a reasonably accurate way of estimating the possible magnitude of earthquakes along faults.

5.4. Lessons for seismic hazard assessment

Two key results have come out of this study that provide new lessons on seismic hazard assessment from paleoearthquake data in the Peruvian Altiplano.

Firstly, there may be a significant preservation bias associated with Holocene normal faults in the Altiplano. Pleistocene glaciation deposited lateral moraines and drift sheets across much of the Altiplano that provide ideal marker surfaces to study faulting, and most of the active faults mapped to date are identified based on offset glacial deposits (e.g. Benavente et al., 2013; Wimpenny et al., 2020). In places where there are no glacial deposits, faults are far more difficult to identify as they have accommodated little finite slip, and fault maps may underestimate the number of potentially seismogenic faults in these areas.

Second, any along-strike variability and segmentation of paleoseismic surface ruptures may not accurately reflect along-strike variations in the earthquake rupture at depth. The surface scarps generated by the Parina earthquake were clearly split into two sections, separated by a gap of ~4 km, despite the slip at depth extending beneath the surface rupture gap. Therefore estimates of the size of past earthquakes based on the along-strike length of their rupture trace must take into account possible gaps caused by near-surface geology.

Surface rupture on shallow, continental faults poses a significant threat for transport infrastructure, villages and critical facilities such as gas pipelines (Baize et al., 2020). In Peru, this surface rupture hazard is rarely taken into account in hazard analyses. Probabilistic and empirical approaches to assessing hazard suffer due to the scarcity of data in the low-to-moderate magnitude range for shallow continental events, and often only consider the effect of the seismic waves. The lack of detailed surface rupture description thus results in poorly-constrained hazard assessment in the high Andes (Yepes et al., 2016) in comparison to our understanding of the hazard posed by megathrust ruptures on the subduction zone (Audin et al., 2008).

6. Conclusions

In this study, we have analysed the heterogeneous surface displacements generated by the moderate-magnitude Parina earthquake in the high Peruvian Andes through a combination of high-resolution DEMs, InSAR data and geological field investigation. We have demonstrated that both late Quaternary slip and the recent Mw 6.1 earthquake have occurred along a newly-identified normal fault, known as the Parina Fault. Similar faults elsewhere in the Peruvian Altiplano may pose a significant seismic hazard to the local population from the effects of shaking on infrastructure and from the secondary hazards of liquefaction and landsliding or rock falls, **particularly in towns and villages sat within hangingwall basins**. However, these faults may be difficult to map in regions where there has been no late Quaternary sedimentation, as the finite extension on the normal faults in the Altiplano is small owing to a recent change in the style of deformation in the region. **In regions where recent fault scarps can be identified,** detailed mapping of the coseismic surface ruptures highlighted that significant along-strike variability in the rupture heights can occur that is not correlated with along-strike changes in the **coseismic** slip pattern at depth, which would imply that trenching a single section of a fault may not accurately

reflect the magnitude of paleo-earthquake offsets on this fault, but could provide evidence on earthquake chronology.

The Parina event is a reminder that **shallow** earthquakes of moderate magnitude pose a real hazard to communities and infrastructure in the Altiplano – possibly greater than megathrust earthquakes on the subduction interface (Costa et al., 2020). The Parina event taught us that the reactivation of these intra-continental faults generates local accelerations >1 g. Many regions exist in the same regime, with little or no geodetically-measurable horizontal deformation, minimal current seismic activity, no documented paleoseismicity and geomorphology that has been shaped by many competing processes – not just faulting (for instance, in the French Alps: *Nocquet* et al., *2016* or in Central USA: *Calais* et al., *2016*). To better assess the seismic hazard in these regions, we must first develop an understanding of how active faulting is recorded in the landscape, both at long and short term.

References

Agisoft, 2017. Agisoft PhotoScan Professional Edition. Agisoft. Retrieved from http ://www.agisoft.com/downloads/installer/, Version 1.4.

Ainscoe, E.A., Abdrakhmatov, K.E., Baikulov, S., Carr, A.S., Elliott, A.J., Grützner, C., Walker, R.T., 2018. Variability in surface rupture between successive earthquakes on the Suusamyr Fault, Kyrgyz Tien Shan: implications for palaeoseismology. Geophys. J. Int. 216, 703–725 https://doi.org/10/ggrm84.

Audin, L., Lacan, P., Tavera, H., Bondoux, F., 2008. Upper plate deformation and seismic barrier in front of Nazca subduction zone: the Chololo Fault System and active tectonics along the Coastal Cordillera, southern Peru. Tectonophysics 459 (1–4), 174–185 https://doi.org/10/b9pr9z.

Baize, S., Nurminen, F., Sarmiento, A., Dawson, T., Takao, M., Scotti, O., et al., 2020. A worldwide and unified database of surface ruptures (SURE) for fault displacement hazard analyses. Seismol Res. Lett. 91 (1), 499–520 https://doi.org/10/ggbdxx.

Bellier, O., Dumont, J.F., Sébrier, M., Mercier, J.L., 1991. Geological constraints on the kinematics and fault-plane solution of the quiches fault zone reactivated during the 10 November 1946 Ancash earthquake, northern Peru. Bull. Seismol. Soc. Am. 81 (2), 468–490.

Benavente, C., Delgado, F., Taipe, E., Audin, L., Pari, W., 2013. *Neotectónica y Peligro Sísmico en el Región Cusco—Boletín Nro 55 Serie C*. INGEMMET. Retrieved from. http://repositorio.ingemmet.gob.pe/handle/ingemmet/296.

Benavente, C., Zerathe, S., Audin, L., Hall, S.R., Robert, X., Delgado, F., et al., 2017. Active transpressional tectonics in the Andean forearc of southern Peru quantified by 10Be surface exposure dating of an active fault scarp: active Tectonics in Southern Peru. Tectonics 36 (9), 1662–1678 https://doi.org/10/gcg5jr.

Cabrera, J., Sébrier, M., 1998. Surface rupture associated with a 5.3-mb earthquake: the 5 April 1986 Cuzco earthquake and kinematics of the Chincheros-Quoricocha faults of the High Andes, Peru. Bull. Seismol. Soc. Am. 88 (1), 242–255.

Calais, E., Camelbeeck, T., Stein, S., Liu, M., Craig, T.J., 2016. A new paradigm for large earthquakes in stable continental plate interiors: LARGE EARTHQUAKES IN SCRs. Geophys. Res. Lett. 43 (20) https://doi.org/10.1002/2016GL070815, 10,621-10,637.

Carlotto, V., 1998. *Evolution andine et raccourcissement au niveau de Cusco (13°-16°S), Pérou: Enregistrement sédimentaire, chronologie, contrôles paléogéographiques, évolution cinématique*. Université Joseph-Fourier - Grenoble I. Retrieved from. https://tel.arch ives-ouvertes.fr/tel-00517507.

Champenois, J., Baize, S., Vallee, M., Jomard, H., Alvarado, A., Espin, P., et al., 2017. Evidences of surface rupture associated with a low-magnitude (Mw 5.0) shallow earthquake in the Ecuadorian Andes: andean earthquake surface rupture.

J. Geophys. Res.: Solid Earth 122 (10), 8446–8458. https://doi.org/10.1002/2017JB013928.

Chiba, T., Kaneta, S., Suzuki, Y., 2008. Red relief image map: new visualization method for three dimensional data. Int. Arch. Photogram. Rem. Sens. Spatial Inf. Sci. 37 (B2), 1071–1076.

Chiba, T., Suzuki, Y., Hiramatsu, T., 2007. Digital terrain representation methods and red relief image map, A new visualization approach. Map J. Jpn. Cartogr. Assoc. 45 (1), 27–36. https://doi.org/10.11212/jjca1963.45.27.

Civico, R., Pucci, S., Villani, F., Pizzimenti, L., De Martini, P.M., Nappi, R., the Open EMERGEO Working Group, 2018. Surface ruptures following the 30 October 2016 Mw 6.5 Norcia earthquake, central Italy. J. Maps 14 (2), 151–160. https://doi.org/10.1080/17445647.2018.1441756.

Clapperton, C.M., 1983. The glaciation of the Andes. Quat. Sci. Rev. 2 (2–3), 83–155.

Costa, C., Alvarado, A., Audemard, F., Audin, L., Benavente, C., Bezerra, F.H., et al., 2020. Hazardous faults of South America; compilation and overview. J. S. Am. Earth Sci. 104, 102837 https://doi.org/10/ghdn5r.

Cowie, P.A., Scholz, C.H., 1992. Growth of faults by accumulation of seismic slip. J. Geophys. Res.: Solid Earth 97 (B7), 11085–11095 https://doi.org/10/ctnv2t.

Ekström, G., Nettles, M., Dziewoński, A.M., 2012. The global CMT project 2004–2010: centroid-moment tensors for 13,017 earthquakes. Phys. Earth Planet. In. 200–201, 1–9 https://doi.org/10/gctpdx.

Ellison, R.A., Klinck, B.A., Hawkins, M.P., 1989. Deformation events in the andean orogenic cycle in the Altiplano and western Cordillera, southern Peru. J. S. Am. Earth Sci. 2 (3), 263–276 https://doi.org/10/bc7f8w.

Ericksen, G.E., Concha, J.F., Silgado, E., 1954. The Cusco, Peru, earthquake of may 21, 1950. Bull. Seismol. Soc. Am. 44 (2A), 97–112.

Fialko, Y., Sandwell, D., Simons, M., Rosen, P., 2005. Three-dimensional deformation caused by the Bam, Iran, earthquake and the origin of shallow slip deficit. Nature 435 (7040), 295–299 https://doi.org/10/fh7bft.

Hubert-Ferrari, A., Armijo, R., King, G., Meyer, B., Barka, A., 2002. Morphology, displacement, and slip rates along the north anatolian fault, Turkey: the north anatolian fault. J. Geophys. Res.: Solid Earth 107 (B10). ETG 9-1-ETG 9-33. https://doi.org/10/cr3t23.

INGEMMET, 2017. GEOCATMIN - SISTEMA DE INFORMACIÓN GEOLÓGICO Y CATASTRAL MINERO. Retrieved from. http://geocatmin.ingemmet.gob.pe.

Jackson, J.A., Gagnepain, J., Houseman, G., King, G.C.P., Papadimitriou, P., Soufleris, C., Virieux, J., 1982. Seismicity, normal faulting, and the geomorphological development of the gulf of corinth (Greece): the corinth earthquakes of february and march 1981. Earth Planet Sci. Lett. 57 (2), 377–397 https://doi.org/10/bbphj4.

Jaillard, E., Santander, G., 1992. La tectonica polifasica en escamas de la zona de Manazo—lagunillas (Puno, sur del Peru). Bulletin de l'Institut Français d'Etudes Andines 21 (1), 37–58.

Khajavi, N., Quigley, M., Langridge, R.M., 2014. Influence of topography and basement depth on surface rupture morphology revealed from LiDAR and field mapping, Hope Fault, New Zealand. Tectonophysics 630, 265–284 https://doi.org/10/f6gcwt.

King, T.R., Quigley, M.C., Clark, D., 2018. Earthquake environmental effects produced by the Mw 6.1, 20th May 2016 Petermann earthquake, Australia. Tectonophysics 747–748, 357–372 https://doi.org/10/ghbhkp.

Llontop, J., Marrou, J., 2016. MOVIMIENTO SISMICO EN LA PROVINCIA DE LAMPA - PUNO (Informe de Emergencia No. 884). COEN - INDECI. Retrieved from. https://www.indeci.gob.pe/objetos/alerta/MjU0Ng==/20161229211000.pdf.

Macharé, J., Escobar, B., Lenin, C., Audin, L., 2009. *Síntesis descriptiva del mapa neotectónico 2008—Boletín Nro 40 Serie C*. INGEMMET. Retrieved from. http://repositorio.ingemmet.gob.pe/handle/ingemmet/245.

Mercier, J.L., Sebrier, M., Lavenu, A., Cabrera, J., Bellier, O., Dumont, J.-F., Machrare, J., 1992. Changes in the tectonic regime above a subduction zone of andean type: the Andes of Peru and Bolivia during the pliocene-pleistocene. J. Geophys. Res. 97 (B8), 11945 https://doi.org/10/dmscwn.

Moss, R.E.S., Stanton, K.V., Buelna, M.I., 2013. The impact of material stiffness on the likelihood of fault rupture propagating to the ground surface. Seismol Res. Lett. 84 (3), 485–488. https://doi.org/10.1785/0220110109.

Nocquet, J.-M., Sue, C., Walpersdorf, A., Tran, T., Lenôtre, N., Vernant, P., et al., 2016. Present-day uplift of the western Alps. Sci. Rep. 6, 28404. https://doi.org/10.1038/srep28404.

Perez, N.D., Horton, B.K., 2014. Oligocene-Miocene deformational and depositional history of the Andean hinterland basin in the northern Altiplano plateau, southern Peru: perez and Horton: N. Altiplano tectonics. Tectonics 33 (9), 1819–1847 https://doi.org/10/f6mw2s.

Philip, H., Megard, F., 1977. Structural analysis of the superficial deformation of the 1969 Pariahuanca earthquakes (Central Peru). Tectonophysics 38, 259–278 https://doi.org/10/cfzqb3.

Pucci, S., De Martini, P.M., Civico, R., Villani, F., Nappi, R., Ricci, T., et al., 2017. Coseismic Ruptures of the 24 August 2016, Mw 6.0 Amatrice Earthquake (Central Italy): M 6 EARTHQUAKE COSEISMIC RUPTURE IN ITALY. Geophysical Research Letters https://doi.org/10/gcpz7f.

Ritz, J.-F., Baize, S., Ferry, M., Larroque, C., Audin, L., Delouis, B., Mathot, E., 2020. Surface rupture and shallow fault reactivation during the 2019 Mw 4.9 Le Teil earthquake, France. Commun. Earth Environ. 1 (1), 10 https://doi.org/10/ghbhsj.

Rodríguez-Pascua, M.A., Silva, P.G., Pérez-López, R., Giner-Robles, J.L., Martín-González, F., Del Moral, B., 2015. Polygenetic sand volcanoes: on the features of liquefaction processes generated by a single event (2012 Emilia Romagna 5.9 Mw earthquake, Italy). Quat. Int. 357, 329–335 https://doi.org/10/f63mm3.

Schwartz, D.P., 1988. Paleoseismicity and neotectonics of the Cordillera blanca fault zone, northern Peruvian Andes. J. Geophys. Res.: Solid Earth 93 (B5), 4712–4730 https://doi.org/10/cmqvtr.

Sébrier, M., Mercier, J.L., Mégard, F., Laubacher, G., Carey-Gailhardis, E., 1985a. Quaternary normal and reverse faulting and the state of stress in the central Andes of south Peru. Tectonics 4 (7), 739–780 https://doi.org/10/dv7bkj.

Sébrier, M., Mercier, J.L., Mégard, F., Laubacher, G., Carey-Gailhardis, E., 1985b. Quaternary normal and reverse faulting and the state of stress in the central Andes of south Peru. Tectonics 4 (7), 739–780 https://doi.org/10/dv7bkj.

Silgado, E., 1978. Historia de los sismos más notables ocurridos en el Perú (1513—1974). *Serie C*. Geodinámica e Ingeniería Geológica, 3.

Stanton, K.V., 2013. Investigation of Parameters Influencing Reverse Fault Rupture Propagation to the Ground Surface. California Polytechnic State University. Retrieved from. http://digitalcommons.calpoly.edu/theses/1145/.

Wells, D.L., Coppersmith, K.J., 1994. New empirical relationships among magnitude, rupture length, rupture width, rupture area, and surface displacement. Bull. Seismol. Soc. Am. 84 (4), 974–1002.

Westoby, M.J., Brasington, J., Glasser, N.F., Hambrey, M.J., Reynolds, J.M., 2012. 'Structure-from-Motion' photogrammetry: a low-cost, effective tool for geoscience applications. Geomorphology 179, 300–314 https://doi.org/10/f4m7ct.

Wimpenny, S., Benavente, C., Copley, A., Garcia, B., Rossell, L., O'Kane, A., Aguirre, E., 2020. Observations and dynamical implications of active normal faulting in south Peru. Geophys. J. Int. ggaa144. https://doi.org/10/ggqtsb.

Wimpenny, S., Copley, A., Benavente, C., Aguirre, E., 2018. Extension and dynamics of the Andes inferred from the 2016 Parina (huarichancara) earthquake. J. Geophys. Res.: Solid Earth 123 (9), 8198–8228, 10/gd4s3s.

Xu, G., Xu, C., Wen, Y., Yin, Z., 2019. Coseismic and postseismic deformation of the 2016 MW 6.2 Lampa earthquake, southern Peru, constrained by interferometric synthetic aperture radar. J. Geophys. Res.: Solid Earth 124 (4), 4250–4272 https://doi.org/10/gfxsdk.

Yepes, H., Audin, L., Alvarado, A., Beauval, C., Aguilar, J., Font, Y., Cotton, F., 2016. A new view for the geodynamics of Ecuador: implication in seismogenic source definition and seismic hazard assessment: Ecuador geodynamics and psha. Tectonics 35 (5), 1249–1279 https://doi.org/10/f8vmj9.